



Article

An Efficient Voltammetric Sensor Based on Graphene Oxide-Decorated Binary Transition Metal Oxides Bi₂O₃/MnO₂ for Trace Determination of Lead Ions

Guangli Li ¹, Xiaoman Qi ¹, Yang Xiao ¹, Yuchi Zhao ¹, Kanghua Li ², Yonghui Xia ³, Xuan Wan ¹, Jingtao Wu ¹ and Chun Yang ^{1,*}

¹ College of Life Sciences and Chemistry, Hunan University of Technology, Zhuzhou 412007, China

² Department of Neurology, Zhuzhou People's Hospital, Zhuzhou 412008, China

³ Zhuzhou Institute for Food and Drug Control, Zhuzhou 412011, China

* Correspondence: yangchunyc@hut.edu.cn

Abstract: Herein we present a facile synthesis of the graphene oxide-decorated binary transition metal oxides of Bi₂O₃ and MnO₂ nanocomposites (Bi₂O₃/MnO₂/GO) and their applications in the voltammetric detection of lead ions (Pb²⁺) in water samples. The surface morphologies, crystal structures, electroactive surface area, and charge transferred resistance of the Bi₂O₃/MnO₂/GO nanocomposites were investigated through the scanning electron microscopy (SEM), power X-ray diffraction (XRD), cyclic voltammetry (CV), and electrochemical impedance spectroscopy (EIS) techniques, respectively. The Bi₂O₃/MnO₂/GO nanocomposites were further decorated onto the surface of a glassy carbon electrode (GCE), and Pb²⁺ was quantitatively analyzed by using square-wave anodic stripping voltammetry (SWASV). We explored the effect of the analytical parameters, including deposition potential, deposition time, and solution pH, on the stripping peak current of Pb²⁺. The Bi₂O₃/MnO₂/GO nanocomposites enlarged the electroactive surface area and reduced the charge transferred resistance by significant amounts. Moreover, the synergistic enhancement effect of MnO₂, Bi₂O₃ and GO endowed Bi₂O₃/MnO₂/GO/GCE with extraordinary electrocatalytic activity toward Pb²⁺ stripping. Under optimal conditions, the Bi₂O₃/MnO₂/GO/GCE showed a broad linear detection range (0.01–10 μM) toward Pb²⁺ detection, with a low limit of detection (LOD, 2.0 nM). The proposed Bi₂O₃/MnO₂/GO/GCE electrode achieved an accurate detection of Pb²⁺ in water with good recoveries (95.5–105%).

Keywords: lead ion; Bi₂O₃; MnO₂; graphene oxide; voltammetric sensor



Citation: Li, G.; Qi, X.; Xiao, Y.; Zhao, Y.; Li, K.; Xia, Y.; Wan, X.; Wu, J.; Yang, C. An Efficient Voltammetric Sensor Based on Graphene Oxide-Decorated Binary Transition Metal Oxides Bi₂O₃/MnO₂ for Trace Determination of Lead Ions. *Nanomaterials* **2022**, *12*, 3317. <https://doi.org/10.3390/nano12193317>

Academic Editor: Fabrizio Pirri

Received: 22 August 2022

Accepted: 20 September 2022

Published: 23 September 2022

Publisher's Note: MDPI stays neutral with regard to jurisdictional claims in published maps and institutional affiliations.



Copyright: © 2022 by the authors. Licensee MDPI, Basel, Switzerland. This article is an open access article distributed under the terms and conditions of the Creative Commons Attribution (CC BY) license (<https://creativecommons.org/licenses/by/4.0/>).

1. Introduction

As a common heavy metal ion (HMI), Pb²⁺ has adverse effects on our health and the environment because of its high toxicity, even at low concentrations. Pb²⁺ in the aquatic environment barely degrades and is easily enriched in aquatic food [1,2]. Therefore, Pb²⁺ chronically endangers human health via the food chain and gradually induces life-threatening circumstances. Excessive levels of Pb²⁺ in human body can severely destroy our organs and nervous system, which is highly associated with various cancers such as lung, kidney, and brain cancers [3]. Hence, a highly efficient determination of Pb²⁺ in water is quite essential to guarantee our health.

Over the last few decades, conventional analytical techniques have been developed to reliably detect Pb²⁺, including X-ray fluorescence spectrometry [4], UV-Vis spectroscopy [5], atomic absorption spectrophotometry [6], inductively coupled plasma mass spectrometry [7], and inductively coupled plasma-atomic emission spectrometry [8]. These analytical techniques are very robust and accurate, even in complex sample matrixes; however, they often require expensive and bulky equipment, cumbersome and time-consuming operation procedures, and highly skilled personnel. Without a doubt, they are not suitable for an

on-field analysis. In recent years, stripping voltammetry, especially SWASV, has emerged as a powerful alternative for the trace determination of HMIs due to its advantages of portability, low cost, rapid response, excellent sensitivity, and feasibility for on-site analyses [9,10]. A voltammetric determination of Pb^{2+} often involves hanging mercury drop electrodes or mercury film electrodes. Owing to their superior stripping characteristics, these mercury-based electrodes are excellent in their sensitivity and reproducibility [11,12]. However, the toxic mercury contaminates samples and poses health risks to analysts. Alternatively, eco-friendly bismuth film electrodes can provide comparable sensing properties for HMI determination [13,14]. Unlike mercury electrodes, bismuth film electrodes usually suffer from surface passivation, which degrades their stripping signals. Therefore, designing novel materials with extraordinary sensing performance toward Pb^{2+} is highly desirable and challenging.

Transition metal oxide nanostructures have been extensively used for the voltammetric detection of HMIs because of their natural abundance, high adsorption capacity, and favorable catalytic activity [15,16]. Among transition metal oxides, MnO_2 has attracted increasing attention due to its earth abundance, low cost, eco-friendliness, favorable electrocatalytic activity, and excellent adsorption capability [17,18]. Nanostructured $\alpha\text{-MnO}_2$ has demonstrated a high affinity for adsorption of Cu^{2+} , Pb^{2+} , Zn^{2+} , Cd^{2+} , Hg^{2+} , etc. [19,20]. Therefore, MnO_2 nanostructures have recently been used for the voltammetric detection of HMIs [21–23]. Owing to its nontoxicity, cost-effectiveness, relatively narrow band gap, high adsorption capacity, and admirable catalytic properties, nanoscale Bi_2O_3 has also found growing interest in various fields such as photocatalysis [24], electroreduction [25], supercapacitors [26–28], and voltammetric sensors [29,30]. It has been reported that nanoscale Bi_2O_3 displayed a high affinity to HMIs such as Cd^{2+} [31,32]. The electrochemical reduction of Bi_2O_3 can produce a porous Bi layer and further form a “fused alloy” with the heavy metal, which accumulates more HMIs on its surface and eventually enhances the sensitivity [33]. For these reasons, Bi_2O_3 -based electrodes have emerged as promising alternatives to mercury-based electrodes for HMI determination.

In contrast to single transition metal oxides, binary transition metal oxide electrocatalysts generally show a higher electrocatalytic activity [34,35]. However, binary transition metal oxides have rarely been used to detect HMIs [36–38]. $\text{Fe}_2\text{O}_3/\text{NiO}$ heterojunctions possess a lower diffusion energy barrier for lead atoms, thus significantly improving the anti-interference ability for detecting Pb^{2+} [37]. $\text{Bi}_2\text{O}_3/\text{Fe}_2\text{O}_3$ -decorated graphene oxide (GO) has demonstrated a remarkable electrocatalytic activity toward Cd^{2+} determination, having a low LOD of 1.85 ng L^{-1} [38]. In our recent work, the synergistic interaction between $\beta\text{-Bi}_2\text{O}_3$ microspheres and shuttle-like $\alpha\text{-Fe}_2\text{O}_3$ nanoparticles enabled the concurrent determination of Cd^{2+} and Pb^{2+} in environmental and food samples at the nanomolar levels [30].

Binary transition metal oxides such as $\text{Bi}_2\text{O}_3/\text{MnO}_2$ have been successfully used in supercapacitors [39,40] and the voltammetric detection of H_2O_2 [41]. In addition, the individual Bi_2O_3 or MnO_2 nanostructures have also been used to detect Pb^{2+} . However, to the best of our knowledge, GO-decorated $\text{Bi}_2\text{O}_3/\text{MnO}_x$ composites have not yet been reported. Herein, we fabricated GO-decorated binary transition metal oxides of Bi_2O_3 and MnO_2 nanocomposites ($\text{Bi}_2\text{O}_3/\text{MnO}_2/\text{GO}$) and used them as a delicate electrocatalyst for Pb^{2+} determination. GO nanoflakes are an electron-rich species that can reduce Pb^{2+} into metallic Pb by applying a suitable potential. In addition, abundant oxygen-containing functional groups (OxFGs) such as carboxyl, hydroxy, carbonyl, and epoxide groups in the edge of GO flakes can firmly bind Pb^{2+} onto their surface through electrostatic and coordination interactions, which facilitates the adsorption of Pb^{2+} [42,43]. Generally, the sensing performance for HMIs mainly relies on the adsorption capacity and electrocatalytic activity of the sensing material that is decorated on the electrode [44], which can be readily tailored using morphology engineering [45,46]. In this regard, we synthesized dandelion-like $\alpha\text{-MnO}_2$ and flower-like $\beta\text{-Bi}_2\text{O}_3$ nanocomposites to enhance the Pb^{2+} adsorption and electrocatalytic activity. With the synergistic interaction of both MnO_2 and Bi_2O_3 , $\text{Bi}_2\text{O}_3/\text{MnO}_2/\text{GO}$

nanocomposites were expected to boost the stripping voltammetric responses of Pb^{2+} . The $\text{Bi}_2\text{O}_3/\text{MnO}_2/\text{GO}$ -modified glassy carbon electrode ($\text{Bi}_2\text{O}_3/\text{MnO}_2/\text{GO}/\text{GCE}$) showed an extraordinary electrocatalytic activity toward the stripping voltammetric behavior of Pb^{2+} , with a wide linear detection range (LDR, 0.01–10 μM), low LOD (2.6 nM), and high sensitivity (53.43 $\mu\text{A } \mu\text{M}^{-1}$). Furthermore, the $\text{Bi}_2\text{O}_3/\text{MnO}_2/\text{GO}/\text{GCE}$ could reliably determine Pb^{2+} in water with good recoveries.

2. Materials and Methods

2.1. Chemicals and Solutions

GO nanoflakes were purchased from Xianfeng Nanotechnology, Inc., (Nanjing, China). Manganese sulfate monohydrate ($\text{MnSO}_4 \cdot \text{H}_2\text{O}$), bismuth nitrate pentahydrate ($\text{Bi}(\text{NO}_3)_3 \cdot 5\text{H}_2\text{O}$), lead nitrate ($\text{Pb}(\text{NO}_3)_2$), potassium peroxydisulfate ($\text{K}_2\text{S}_2\text{O}_8$), potassium sulfate (K_2SO_4), N, N-dimethylformamide (DMF), potassium ferri/ferro-cyanide ($\text{K}_{3/4}[\text{Fe}(\text{CN})_6]$), sodium acetate (NaAc), acetic acid (HAc), concentrated H_2SO_4 , and anhydrous alcohol were purchased from Sinopharm Chemical Reagent Co., Ltd. (Shanghai, China). All reagents were of analytical grade and directly used as received. Water samples were collected from a local lake and from our laboratory. 0.3312 g of $\text{Pb}(\text{NO}_3)_2$ was completely dissolved in 100 mL of 0.1 M HAc-NaAc buffer (pH = 5.5) to prepare a 0.01 M Pb^{2+} stock solution. A series of standard solutions of Pb^{2+} with different concentrations were prepared by appropriately diluting the stock solution with the 0.1 M HAc-NaAc buffer (pH = 5.5). Deionized water (DI water, resistivity of 18.2 $\text{M}\Omega \cdot \text{m}$) was used for all experiments.

2.2. Preparation of $\text{Bi}_2\text{O}_3/\text{MnO}_2/\text{GO}$ Nanocomposites

2.2.1. Preparation of Dandelion-like $\alpha\text{-MnO}_2$ Microspheres

Dandelion-like $\alpha\text{-MnO}_2$ microspheres were prepared via a facile hydrothermal treatment route [47]. Typically, 1.3522 g of $\text{MnSO}_4 \cdot \text{H}_2\text{O}$, 2.1626 g of $\text{K}_2\text{S}_2\text{O}_8$ and 1.3941 g of K_2SO_4 were sequentially added to 60 mL of 0.6 M H_2SO_4 and magnetically stirred for 30 min to completely dissolve. Then, the mixture solution was decanted into a 100 mL Teflon-lined stainless steel container and heated at a temperature of 140 °C for 12 h. The resultant product was repeatedly rinsed with DI water and dried at 60 °C overnight for further use.

2.2.2. Synthesis of Flower-like $\beta\text{-Bi}_2\text{O}_3$ Microspheres

Flower-like $\beta\text{-Bi}_2\text{O}_3$ microspheres were synthesized by a simple hydrothermal treatment followed by a thermal decomposition at high temperature [30]. In brief, 0.03 mol of $\text{Bi}(\text{NO}_3)_3 \cdot 5\text{H}_2\text{O}$ was dissolved into 11 mL of HAc, and 14 mL of anhydrous ethanol was then added to form a white suspension. The resulting suspension was ceaselessly stirred for 45 min, and 28 mL of DMF was then added to yield a clear solution. Subsequently, the mixture solution was poured into a 100 mL Teflon-lined stainless steel autoclave and reacted at a temperature of 120 °C for 40 min. The precursor was centrifuged at 10,000 rpm for 5 min, where it was alternately rinsed with anhydrous alcohol and DI water and allowed to dry at 80 °C overnight. Finally, the resultant $\beta\text{-Bi}_2\text{O}_3$ precursor was further transferred to a porcelain boat and calcinated at 350 °C for 4 h at a heating rate of 2 °C min^{-1} in an air atmosphere to yield orange-yellow $\beta\text{-Bi}_2\text{O}_3$ microspheres.

2.2.3. Preparation of $\text{Bi}_2\text{O}_3/\text{MnO}_2/\text{GO}$ Nanocomposites

At first, 5 mg of dandelion-like $\alpha\text{-MnO}_2$ microspheres, flower-like $\beta\text{-Bi}_2\text{O}_3$ microspheres, and GO nanoflakes were separately dispersed into 10 mL of DI water under ultrasonication to form their respective uniform dispersions at a concentration of 0.5 mg mL^{-1} . Then, 1 mL of the $\alpha\text{-MnO}_2$, $\beta\text{-Bi}_2\text{O}_3$, and GO dispersions were further mixed and subjected to a 30 min ultrasonication to obtain a uniform $\text{Bi}_2\text{O}_3/\text{MnO}_2/\text{GO}$ dispersion. The amount of the three materials were optimized during our preliminary experiments. $\text{Bi}_2\text{O}_3/\text{MnO}_2/\text{GO}$ composites containing 5 mg of each of the three materials showed the largest stripping

peak current of Pb^{2+} . Therefore, we selected the composite with this component content as the sensing material.

2.3. Characterizations of Sensing Materials

The microscopic morphologies of the GO nanoflakes, dandelion-like $\alpha\text{-MnO}_2$ microspheres, flower-like $\beta\text{-Bi}_2\text{O}_3$ microspheres, and $\text{Bi}_2\text{O}_3/\text{MnO}_2/\text{GO}$ nanocomposites were observed using field-emission SEM (Sigma HD, Zeiss, Oberkochen, Germany). Before taking the SEM measurements, a few thin layers of Au were coated onto the surface of the samples. The crystalline structures of these materials were studied using a powder XRD (Rigaku Ultima IV, Tokyo, Japan) with monochromatized Cu $K\alpha$ radiation ($\lambda = 1.54 \text{ \AA}$).

2.4. Fabrication of Modified Electrodes

Before electrode modification, the GCE was thoroughly polished to a shining mirror-like surface with $0.05 \mu\text{m}$ of alumina slurry, and it was ultrasonically cleaned with anhydrous alcohol and DI water for three cycles to remove residual contaminants. Then, the polished GCE was exposed to infrared light to allow the material to adequately dry. The $\text{Bi}_2\text{O}_3/\text{MnO}_2/\text{GO}/\text{GCE}$ electrode was prepared by using a conventional drop-casting method. Specifically, $5 \mu\text{L}$ of the $\text{Bi}_2\text{O}_3/\text{MnO}_2/\text{GO}$ dispersion was cast on the surface of the freshly polished GCE and dried under the exposure of infrared light to form a firm sensing film. For comparison, the $\text{MnO}_2/\text{GO}/\text{GCE}$, $\text{Bi}_2\text{O}_3/\text{GO}/\text{GCE}$, and GO/GCE were also fabricated using the same procedure, aside from the dispersion used.

2.5. Electrochemical Measurements

All electrochemical measurements were performed on a CHI 660E electrochemical workstation (Chenhua Inc., Shanghai, China) equipped with a classic three-electrode system, which consists of the $\text{Bi}_2\text{O}_3/\text{MnO}_2/\text{GO}/\text{GCE}$ electrode, a Pt wire, and a saturated calomel electrode (SCE) as the working, counter, and reference electrodes, respectively. A 10 mL electrochemical cell made of glass was used for the electrochemical measurements. Unless otherwise specified, the 0.1 M HAc-NaAc buffer ($\text{pH} = 5.5$) functioned as the supporting electrolyte. To assess the electrochemical performance, the CV curves and Nyquist plots of different modified electrodes were recorded in a solution of 2 mM $[\text{Fe}(\text{CN})_6]^{3-/4-}$ and 0.1 M KCl. To improve the stripping responses, a suitable deposition was employed in the Pb^{2+} standard solutions. After 30 s of rest, the stripping peak currents of Pb^{2+} were recorded between -1.0 V and -0.5 V using the SWASV technique. The frequency, step potential, and pulse amplitude of the SWASV were set at 15 Hz, 4 mV, and 25 mV, respectively. When not in use, the $\text{Bi}_2\text{O}_3/\text{MnO}_2/\text{GO}/\text{GCE}$ electrode was stored in the air. After each determination, the electrode surface was refreshed by immersing it into a blank solution and applying $+0.3 \text{ V}$ for 150 s to ensure the complete removal of the residual metals.

3. Results and Discussion

3.1. Physical Characterization

The microscopic morphologies of the GO nanoflakes, dandelion-like $\alpha\text{-MnO}_2$ microspheres, flower-like $\beta\text{-Bi}_2\text{O}_3$ microspheres, and $\text{Bi}_2\text{O}_3/\text{MnO}_2/\text{GO}$ nanocomposites were observed using the SEM technique, and their SEM images are shown in Figure 1. The GO nanosheets exhibited a typical lamellar structure with obvious wrinkles (Figure 1A). Dandelion-like nanostructures are found in the image of the $\alpha\text{-MnO}_2$, consisting of many radially distributed nanorods (Figure 1B). Typical flower-like $\beta\text{-Bi}_2\text{O}_3$ microspheres are observed in Figure 1C, which consist of many interconnected thin nanosheets. The unique dandelion-like $\alpha\text{-MnO}_2$ and flower-like Bi_2O_3 structures enlarge the electroactive surface area, thereby improving the sensing performance. In addition, the interconnected porous microstructures are found in the dandelion-like $\alpha\text{-MnO}_2$ and flower-like Bi_2O_3 microspheres, which facilitate the electrolyte infiltration and adsorption of HMIs. As illustrated in Figure 1D, typical microspheres are observed in the SEM image of the $\text{Bi}_2\text{O}_3/\text{MnO}_2/\text{GO}$ nanocomposites. In addition, the microspheres are partially wrapped by GO nanosheets.

To conform the composition of the microspheres, the energy-dispersive X-ray spectroscopy (EDS) mappings of the $\text{Bi}_2\text{O}_3/\text{MnO}_2/\text{GO}$ nanocomposites were also measured (Figure 1E). The uniformly dispersed C, O, Mn, and Bi distribution suggests the presence of C, O, Mn, and Bi elements. In addition, the distributions of Mn and Bi exhibit obvious microsphere structures, indicating that the microsphere consists of both Bi_2O_3 and MnO_2 . All of these results indicate the successful synthesis of $\text{Bi}_2\text{O}_3/\text{MnO}_2/\text{GO}$ nanocomposites.

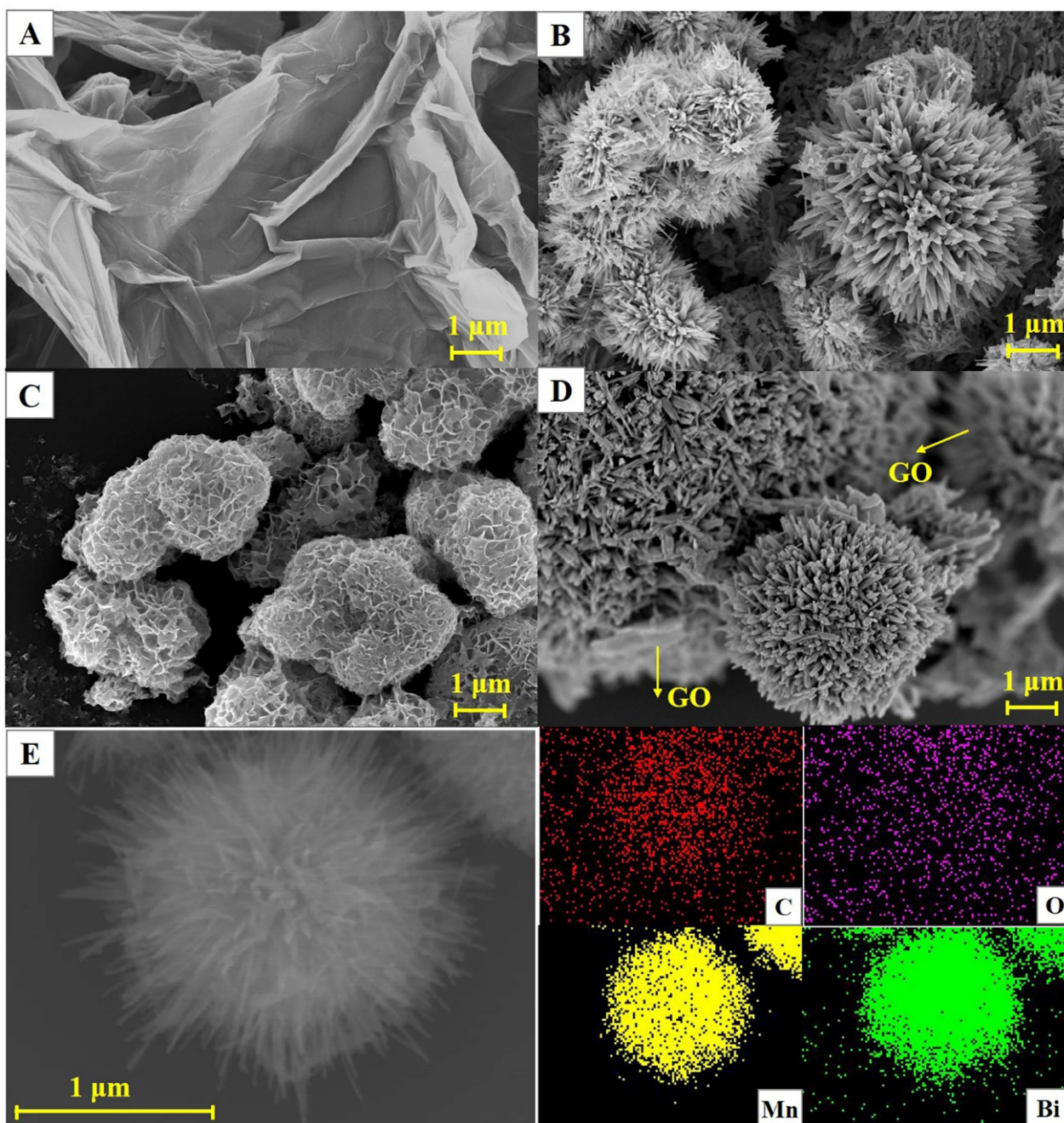


Figure 1. SEM images of the GO nanoflakes (A), dandelion-like $\alpha\text{-MnO}_2$ microspheres (B), flower-like $\beta\text{-Bi}_2\text{O}_3$ microspheres (C), and $\text{Bi}_2\text{O}_3/\text{MnO}_2/\text{GO}$ nanocomposites (D). (E) EDS mapping of the $\text{Bi}_2\text{O}_3/\text{MnO}_2/\text{GO}$ nanocomposites.

Figure 2 displays the XRD patterns of the GO nanoflakes, dandelion-like $\alpha\text{-MnO}_2$ microspheres, flower-like $\beta\text{-Bi}_2\text{O}_3$ microspheres, and $\text{Bi}_2\text{O}_3/\text{MnO}_2/\text{GO}$ nanocomposites. A sharp diffraction peak was observed at 2θ of 9.68° in the XRD pattern of the GO, which is attributed to the (001) crystal plane of the GO [48]. $\alpha\text{-MnO}_2$ nanostructures displayed

distinct diffraction peaks at 2θ of 12.78° , 18.08° , 28.64° , 37.62° , 50° , 56.14° , 60.18° , and 69.54° , corresponding to the (110), (200), (310), (211), (411), (600), (521), and (541) planes of α - MnO_2 (JCPDS 440141), respectively [49]. Additionally, we detected sharp diffraction peaks without any apparent impurity peaks, demonstrating that the as-prepared α - MnO_2 microspheres were of high purity. Broad diffraction peaks were observed for the flower-like β - Bi_2O_3 at 28.00° , 32.52° , 46.32° , and 55.64° , which can be indexed to the (201), (220), (222), and (213) crystal facets (JCPDS 651209) [24]. The characteristic diffraction peaks of both the GO α - MnO_2 and β - Bi_2O_3 can be observed in the XRD pattern of the $\text{Bi}_2\text{O}_3/\text{MnO}_2/\text{GO}$ nanocomposites. However, the intensity of the diffraction peaks of the α - MnO_2 and β - Bi_2O_3 microspheres were significantly weakened, which was mainly due to the presence of a large amount of GO partially masking the diffraction peaks of the α - MnO_2 and β - Bi_2O_3 . This further confirmed that the $\text{Bi}_2\text{O}_3/\text{MnO}_2/\text{GO}$ nanocomposites were successfully synthesized.

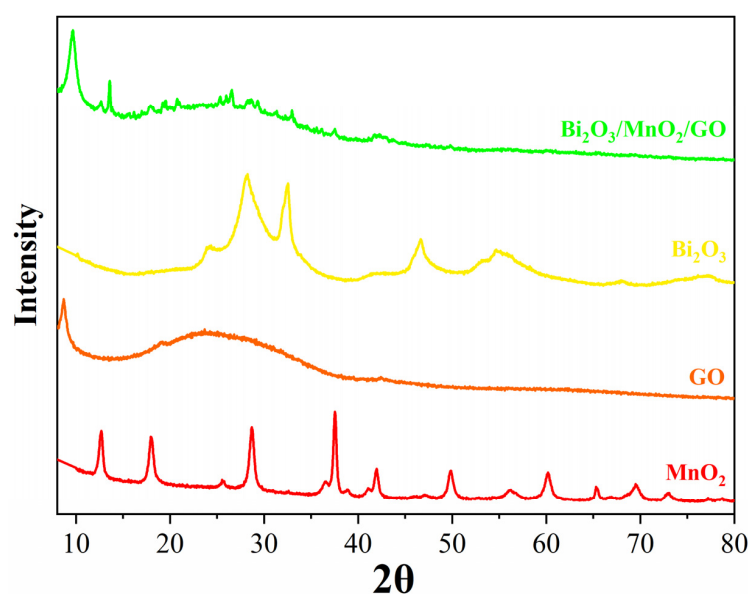


Figure 2. XRD pattern of the GO nanoflakes, dandelion-like α - MnO_2 microspheres, flower-like β - Bi_2O_3 microspheres, and $\text{Bi}_2\text{O}_3/\text{MnO}_2/\text{GO}$ nanocomposites.

3.2. Electrochemical Properties of Different Electrodes

The CV curves for the different electrodes were scanned in a solution of 2.0 mM $[\text{Fe}(\text{CN})_6]^{3-/4-}$ and 0.1 M KCl to assess their electrochemical properties. As shown in Figure 3A, a pair of sharp and symmetric redox peaks occur at all electrodes, with an almost identical anodic and cathodic peak current (I_{pa} and I_{pc}), indicating that the redox of Fe(III)/Fe(II) is a quasi-reversible process. After the modification of the GO, $\text{Bi}_2\text{O}_3/\text{GO}$, MnO_2/GO and $\text{MnO}_2/\text{Bi}_2\text{O}_3/\text{GO}$, the redox peak currents were sequentially enhanced. The corresponding effective electroactive areas were also estimated based on the Randles–Sevcik equation:

$$I_{pc} = 2.69 \times 10^5 \times n^{\frac{3}{2}} v^{\frac{1}{2}} D^{\frac{1}{2}} AC^0 \quad (1)$$

$$R_f = \frac{A}{A_{\text{geom}}} \quad (2)$$

where A is the effective electroactive area, A_{geom} is the geometric surface area (diameter of 3.0 mm, 7.07 mm^2), and the other symbols retain their usual meanings. The effective electroactive area and roughness factor of these electrodes were estimated according to Equations (1) and (2) (Table 1). The effective electroactive area of the bare GCE was very close to its actual geometric area. The effective electroactive area of the $\text{Bi}_2\text{O}_3/\text{MnO}_2/\text{GO}/\text{GCE}$ was 1.8 and 1.6 times greater than that of the bare GCE and GO/GCE , respectively. This indicates that the $\text{Bi}_2\text{O}_3/\text{MnO}_2/\text{GO}$ nanocomposites signifi-

cantly boosted the electroactive surface area, which is closely related to the high specific area of the GO, dandelion-like MnO_2 , and flower-like Bi_2O_3 nanostructures. The large electroactive surface area of the $\text{Bi}_2\text{O}_3/\text{MnO}_2/\text{GO}$ not only increases the accessible catalytic active sites, but also facilitates the adsorption of more Pb^{2+} , which ultimately results in the improvement of the Pb^{2+} sensing performance.

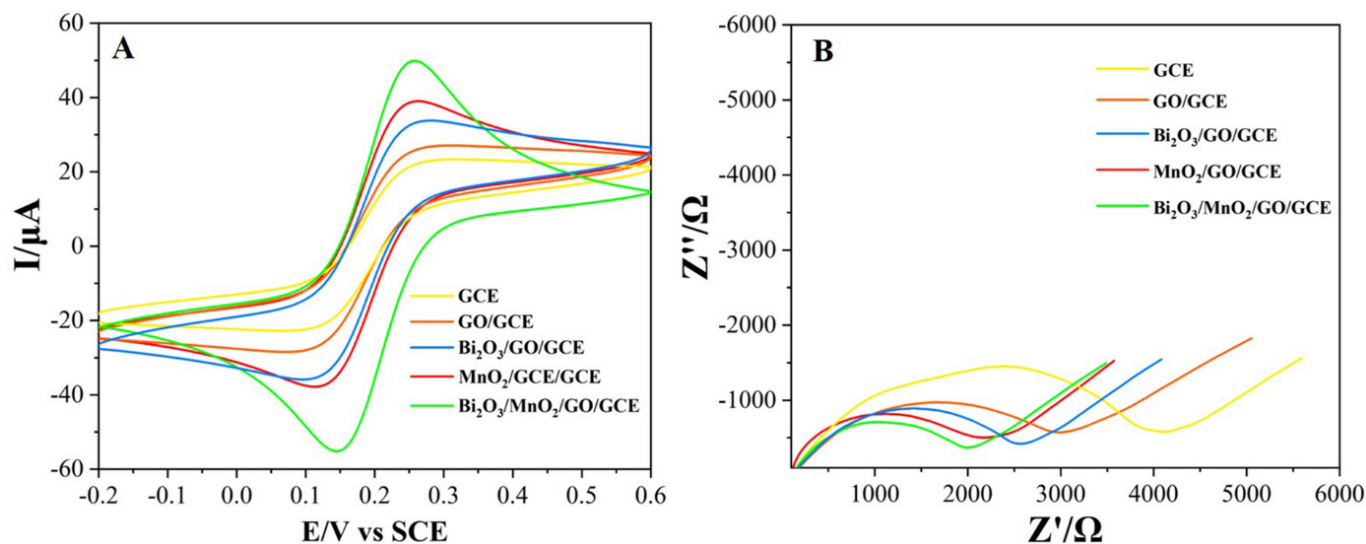


Figure 3. The CV curves (A) and Nyquist plots (B) of the bare GCE, GO/GCE, $\text{Bi}_2\text{O}_3/\text{GO}/\text{GCE}$, $\text{MnO}_2/\text{GO}/\text{GCE}$, and $\text{Bi}_2\text{O}_3/\text{MnO}_2/\text{GO}/\text{GCE}$ recorded in a 10 mL solution of 2.0 mM $[\text{Fe}(\text{CN})_6]^{3-/4-}$ and 0.1 M KCl.

Table 1. A comparison of the electrochemical properties of different electrodes.

| Electrode | I_{pc} | Electroactive Area | Roughness Factor | R_{ct} |
|---|---------------------|---------------------|------------------|---------------|
| GCE | 32.83 μA | 7.00 mm^2 | 0.990 | 4126 Ω |
| GO/GCE | 35.86 μA | 7.65 mm^2 | 1.082 | 2815 Ω |
| $\text{Bi}_2\text{O}_3/\text{GO}/\text{GCE}$ | 44.58 μA | 9.50 mm^2 | 1.344 | 2632 Ω |
| $\text{MnO}_2/\text{GO}/\text{GCE}$ | 48.94 μA | 10.43 mm^2 | 1.475 | 1898 Ω |
| $\text{Bi}_2\text{O}_3/\text{MnO}_2/\text{GO}/\text{GCE}$ | 58.94 μA | 12.57 mm^2 | 1.778 | 1761 Ω |

EIS is a useful technique to assess the interfacial properties, mass-transport, and kinetic parameters, in addition to the charge transferred resistance (R_{ct}) of electrodes by observing the change in a semicircle diameter [50–52]. Figure 3B displays the Nyquist plots of the different electrodes. Typically, a Nyquist diagram includes a semicircle at the higher frequency domain and a straight line at the lower frequency region, which is closely related to the electron-transfer-limited and diffusion-controlled processes, respectively [53,54]. Clearly, the bare GCE showed the largest semicircle ($R_{ct} = 4126 \Omega$), suggesting that the electron transfer was severely retarded in the unmodified bare. When GO was decorated on the GCE, the R_{ct} reduced to 2815 Ω due to the good electrical conductivity of GO. When the β - Bi_2O_3 and α - MnO_2 microspheres were further introduced into the GO/GCE, the respective R_{ct} reduced to 2632 Ω and 1898 Ω , respectively. As anticipated, the smallest semicircle diameter was achieved in the $\text{Bi}_2\text{O}_3/\text{MnO}_2/\text{GO}/\text{GCE}$ ($R_{ct} = 1761 \Omega$). This indicates that the $\text{Bi}_2\text{O}_3/\text{MnO}_2/\text{GO}$ effectively promotes the electron transfer, which ultimately improves the electrochemical sensing performance.

3.3. Stripping Voltammetric Responses of Pb^{2+} on Different Electrodes

The voltammetric behavior of 1.0 μM of Pb^{2+} on the different modified electrodes were studied using the SWASV technique (Figure 4). As a control, we also recorded the SWASV curves of the different electrodes in the absence of Pb^{2+} . In the absence of Pb^{2+} , no noticeable

response peaks were found in any of the electrodes (Figure S1). In unmodified GCE, a weak stripping peak was observed at -0.656 V with an anodic stripping peak current (I_{pa}) of 4.118 μ A, indicating that a sluggish oxidation process occurred in unmodified GCE. When GO nanoflakes were decorated on the GCE surface, the I_{pa} (Pb^{2+}) increased to 6.277 μ A because GO, with its large surface area and abundant OXFGs, facilitates the adsorption of Pb^{2+} . When the flower-like β - Bi_2O_3 and dandelion-like α - MnO_2 microspheres were introduced into the GO/GCE, their I_{pa} (Pb^{2+}) significantly increased to 9.541 μ A and 10.95 μ A, respectively, while their respective anodic stripping peak potentials (E_{pa}) also decreased. This suggests that the decoration of flower-like β - Bi_2O_3 and dandelion-like α - MnO_2 microspheres promotes an efficient electron transfer, which is closely related to high affinity capacity and extraordinary electrocatalytic activity toward Pb^{2+} . As expected, the GO-coated binary transition metal oxides of Bi_2O_3/MnO_2 remarkably improved the stripping voltammetric response of Pb^{2+} , with the highest I_{pa} of 58.07 μ A and the lowest E_{pa} (-0.667 V). Notably, the stripping peak current for the GO-coated binary transition metal oxide was about five times higher than that of the GO-coated single metal oxides, suggesting that the synergistic effect between the flower-like β - Bi_2O_3 and dandelion-like α - MnO_2 microspheres is attributed to the enhanced I_{pa} and reduction in overpotential.

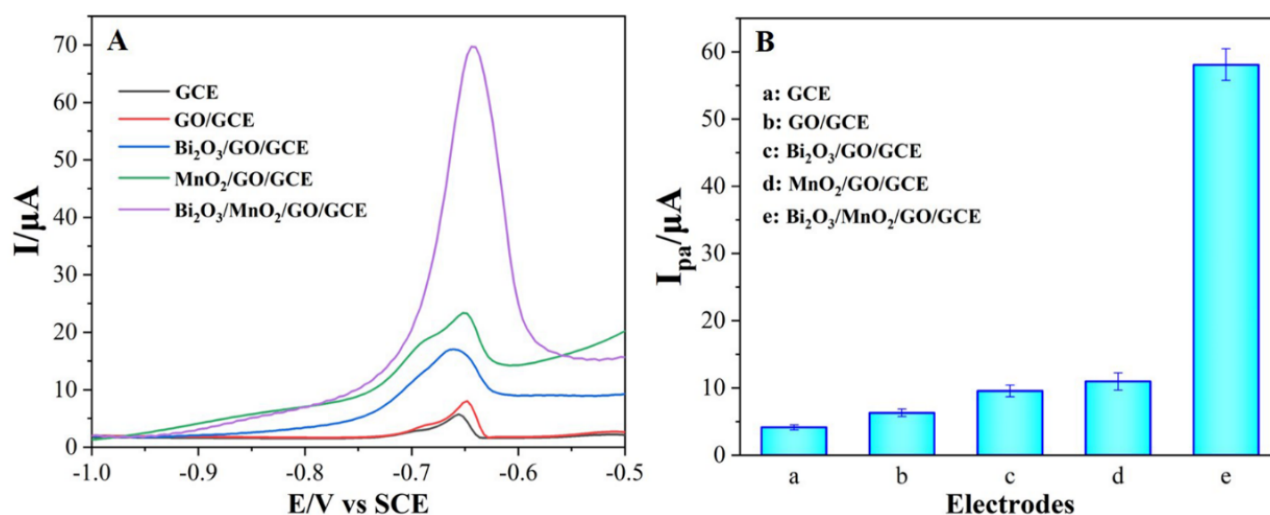


Figure 4. The SWASV curves (A) and their respective stripping peak currents (B) of Pb^{2+} , measured on different electrodes in 10 mL of 0.1 M HAc-NaAc buffer (pH = 5.5) containing 1.0 μ M of Pb^{2+} . Deposition was applied at -1.0 V for 300 s.

3.4. Optimization of Determination Conditions

3.4.1. Effect of Deposition Parameters

Deposition parameters have a prominent effect on the voltammetric behavior of Pb^{2+} . As illustrated in Figure 5A, the I_{pa} (Pb^{2+}) gradually increased when the deposition potential shifted from -1.3 V to -1.0 V, then sharply declined as the deposition potentials shifted further. At an excessively negative deposition potential, hydrogen bubbles would be generated on the surface of the $Bi_2O_3/MnO_2/GO/GCE$, resulting in the exfoliation of the deposited Pb^{2+} . When the deposition potential was higher than -1.0 V, the electrochemical energy was not sufficient to reduce the deposited Pb^{2+} . Therefore, the optimal deposition potential was set at -1.0 V. Generally, prolonging the deposition time can enhance the adsorption amount of HMIs on the electrode surface, thereby increasing the stripping peak current. As presented in Figure 5B, the I_{pa} (Pb^{2+}) steadily increased with deposition time until reaching a plateau at 300 s. This was mainly because the surface adsorption sites of the $Bi_2O_3/MnO_2/GO/GCE$ were saturated at 300 s. Thus, the optimum deposition time was set at 300 s.

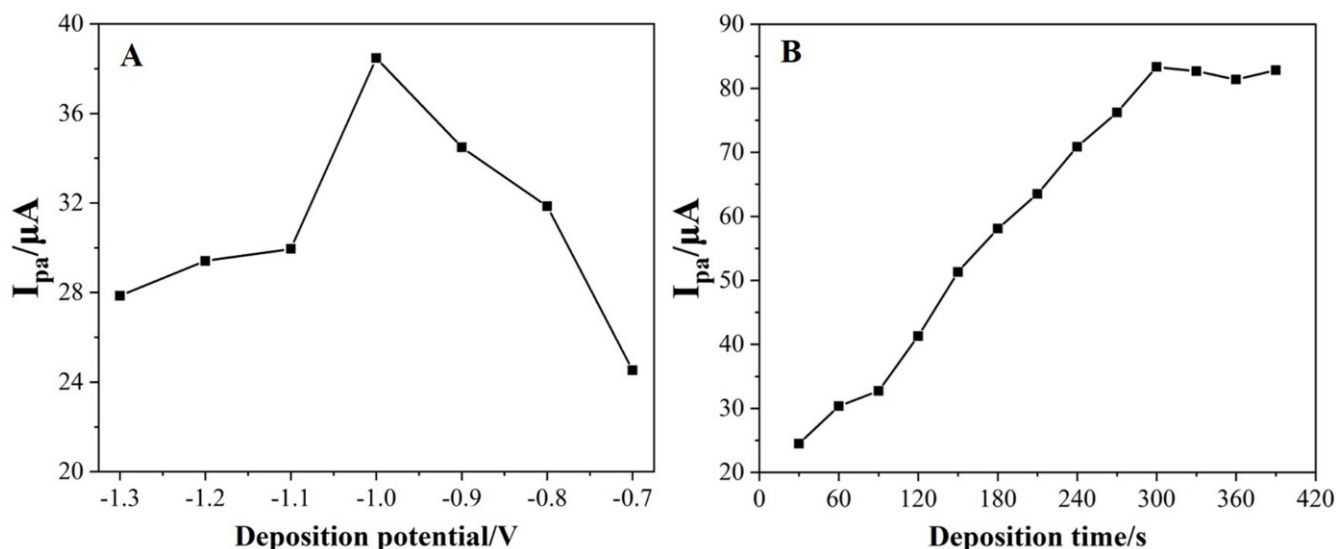


Figure 5. (A) The effect of the deposition potential on the I_{pa} of 1.0 μM of Pb^{2+} with the deposition time fixed at 120 s. (B) The effect of the deposition time on the I_{pa} of 1.0 of μM Pb^{2+} with the deposition potential fixed at -1.0 V.

3.4.2. Effect of Solution pH

It is well-known that a solution's pH has a significant impact on the I_{pa} (Pb^{2+}). Therefore, the influence of the solution's pH was also explored. As illustrated in Figure 6, the I_{pa} (Pb^{2+}) slowly increased as the pH increased from 3.0 to 4.5, and then sharply increased until the pH of 5.5. Afterwards, the I_{pa} (Pb^{2+}) dramatically decreased when the pH exceeded 5.5. Therefore, pH = 5.5 was chosen as the optimal solution pH. This phenomenon can be interpreted as follows. At lower pH values, the H^+ adsorption on the electrode surface neutralizes the negative charge on the electrode surface, which reduces the adsorption of Pb^{2+} , resulting in a decrease in the I_{pa} (Pb^{2+}). Pb^{2+} tends to be hydrolyzed in a solution with a higher pH so that the concentration of free Pb^{2+} in the solution decreases and the I_{pa} (Pb^{2+}) decreases.

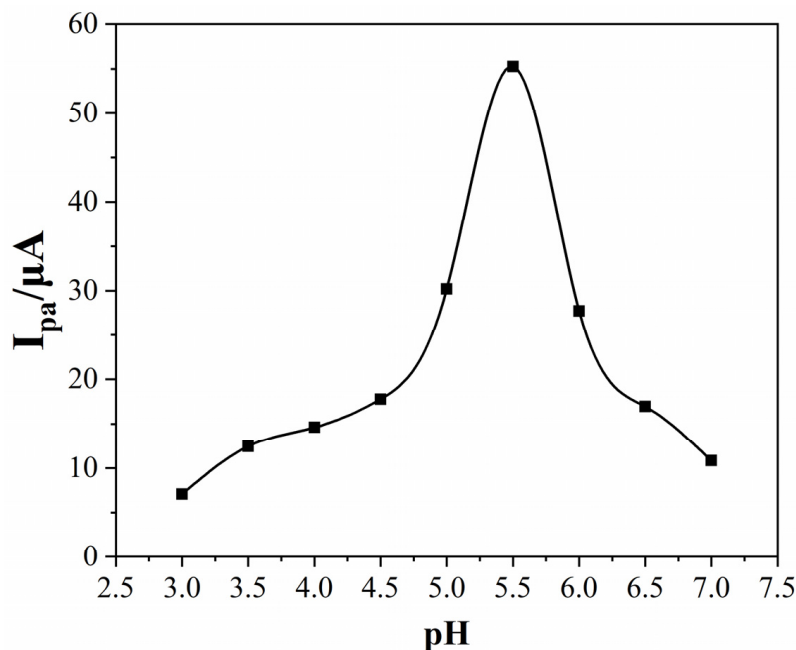


Figure 6. The effect of the solution pH on the I_{pa} of 1.0 μM of Pb^{2+} . Deposition was applied at -1.0 V for 300 s.

3.5. Stripping Kinetics of Pb^{2+} on the $Bi_2O_3/MnO_2/GO/GCE$

In order to study the stripping kinetics of Pb^{2+} , the cyclic voltammograms of $1.0 \mu M$ of Pb^{2+} were measured by the $Bi_2O_3/MnO_2/GO/GCE$ at different scanning rates ($0.05\text{--}0.40 \text{ V s}^{-1}$). Figure 7A shows the CV curves of $1.0 \mu M$ of Pb^{2+} at various scanning rates. A pair of well-shaped redox peaks occurred at all scanning rates with almost identical I_{pa} and I_{pc} ($I_{pa}/I_{pc} \approx 1$), suggesting that Pb^{2+} stripping is a quasi-reversible process. As the scanning rate increased, the I_{pa} and I_{pc} gradually increased. In addition, the anodic peaks shift to more positive potential while the cathodic peaks shift to more negative potential. As illustrated in Figure 7B, both the I_{pa} and I_{pc} are linearly correlated to the square root of scanning rates ($v^{1/2}$), demonstrating that Pb^{2+} stripping was primarily controlled by the diffusion.

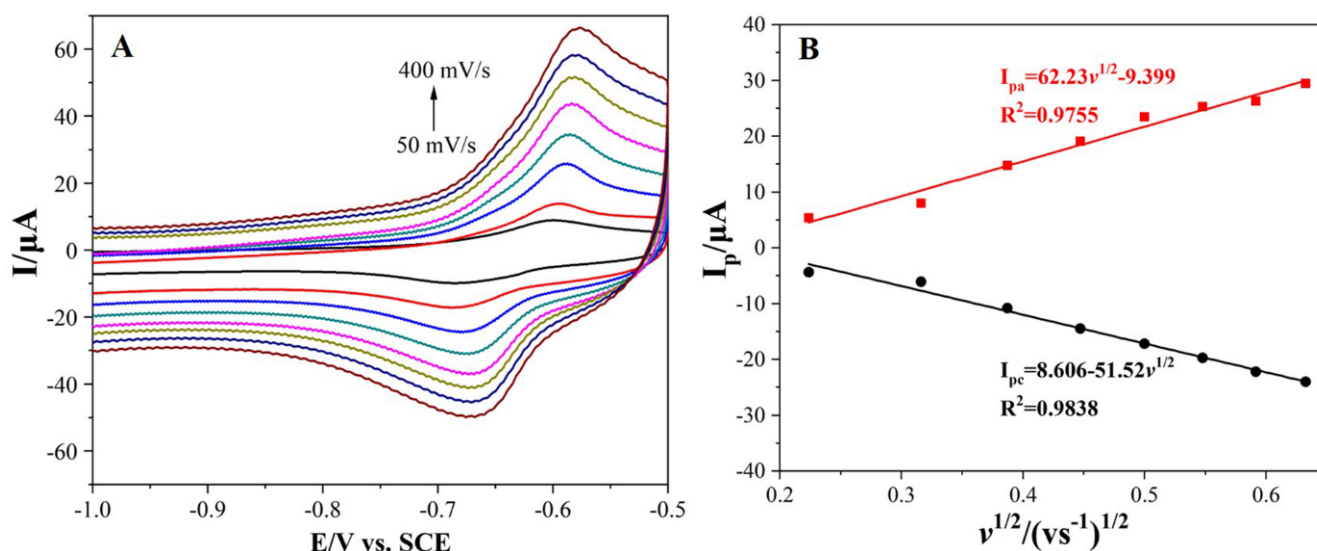


Figure 7. (A) The CV curves of Pb^{2+} recorded at various scanning rates in 10 mL of 0.1 M HAc-NaAc buffer (pH = 5.5) containing $1.0 \mu M$ of Pb^{2+} . (B) A linear plot of I_{pa} (Pb^{2+}) versus square root of scanning rate ($v^{1/2}$).

3.6. Calibration Plot, LDR, and LOD

Under optimal determination conditions, the I_{pa} (Pb^{2+}) at various concentrations were measured on the $Bi_2O_3/MnO_2/GO/GCE$ via the SWASV technique. As illustrated in Figure 8A, well-defined stripping peaks of Pb^{2+} occurred at about -0.65 V with a slight positive shift at higher concentrations. As shown in the inset of Figure 8A, the stripping peaks of low concentrations of Pb^{2+} slightly shifted to more negative biases, probably due to the electrode surfaces not being exactly the same. However, the obvious positive shift in the peak potential at higher concentrations is probably due to the occurrence of concentration polarization. Moreover, the I_{pa} (Pb^{2+}) gradually increased with Pb^{2+} concentration. The I_{pa} (Pb^{2+}) are in good proportion to Pb^{2+} concentration from 0.01 to $10 \mu M$ (Figure 8B). The corresponding linear regression equation was expressed as $I_{pa}(\mu A) = 53.45C(\mu M) + 0.578$, with a good correlation coefficient (R^2) of 0.998. The LOD was calculated as 2.0 nM ($0.41 \mu g L^{-1}$) based on $3\sigma/s$ (where σ is the standard deviation in blank solution and s is the slope of the calibration plot). A comparison of the analytical properties for Pb^{2+} was also made between the $Bi_2O_3/MnO_2/GO/GCE$ composite and previously reported ones. As shown in Table 2, the analytical properties of the $Bi_2O_3/MnO_2/GO/GCE$ composite, including the LDR, LOD, and sensitivity, well matches or even exceeds the previously reported electrodes.

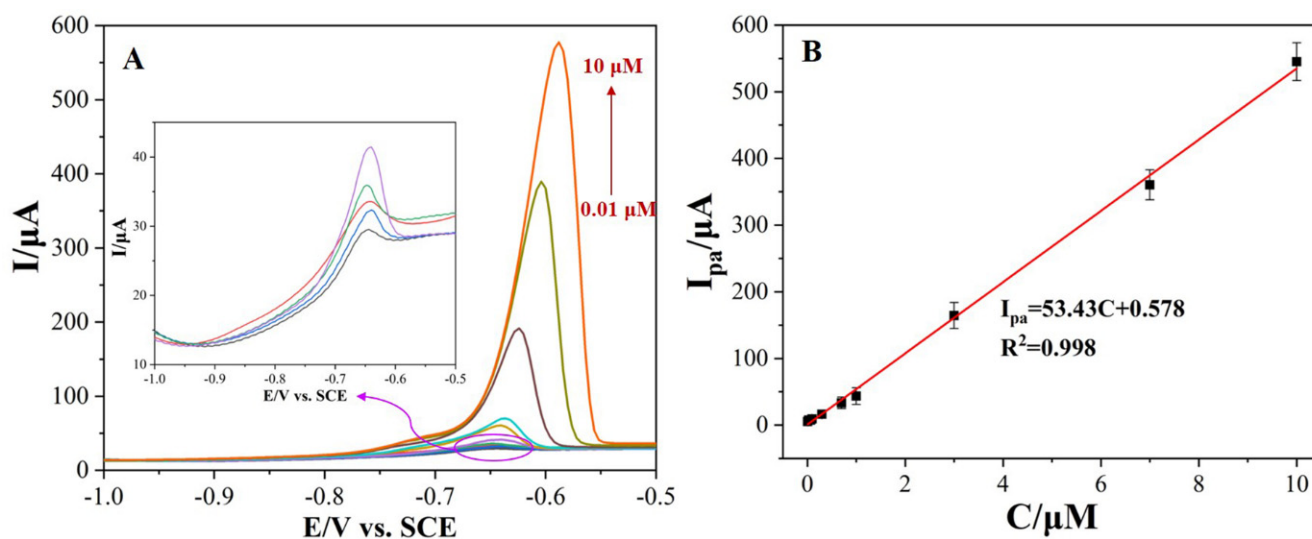


Figure 8. (A) The SWASV curves of Pb^{2+} recorded on the $\text{Bi}_2\text{O}_3/\text{MnO}_2/\text{GO}/\text{GCE}$ in 10 mL of 0.1 M HAc-NaAc buffer (pH = 5.5) containing various concentrations of Pb^{2+} ; the inner inset represents the magnification of the SWASV curves of Pb^{2+} at low concentration (0.01–1.0 μM). (B) A linear plot of the SWASV responses of Pb^{2+} versus Pb^{2+} concentration.

Table 2. A comparison on the analytical properties for Pb^{2+} determination.

| Electrodes | Method | LDR ($\mu\text{g L}^{-1}$) | LOD ($\mu\text{g L}^{-1}$) | Refs. |
|---|--------|---------------------------------|---------------------------------|-----------|
| $\alpha\text{-Fe}_2\text{O}_3/\text{NiO}/\text{GCE}$ | SWASV | 10.4–186 | 4.14 | [37] |
| $\text{BiF}/\text{ERGO}/\text{SPE}$ | SWASV | 1.00–60.0 | 0.80 | [55] |
| $\text{Fe}_3\text{O}_4/\text{Bi}_2\text{O}_3/\text{C}_3\text{N}_4/\text{GCE}$ | SWASV | 2.07–622 | 0.21 | [36] |
| $\text{SnS-Bi}_2\text{O}_3/\text{GCE}$ | SWASV | 20.7–207 | 0.29 | [16] |
| L-Cys/GR-CS/GCE | DPASV | 1.04–64.1 | 0.12 | [56] |
| SWCNHs/SPE | SWASV | 1.0–60.0 | 0.40 | [57] |
| $\text{Bi}_2\text{O}_3/\text{CPE}$ | DPASV | 10.0–100 | 5.00 | [32] |
| $\text{Fe}_3\text{O}_4@\text{G2-PAD}/\text{CPE}$ | SWASV | 0.50–80.0 | 0.17 | [58] |
| $\text{g-C}_3\text{N}_4/\text{r-GO}/\text{GCE}$ | SWASV | 1.00–300 | 0.15 | [59] |
| L-cysine/Au@SiO ₂ | SWASV | 5.00–80 | 0.60 | [60] |
| @Fe ₃ O ₄ /NG/GCE | SWASV | 5.00–80 | 0.60 | [60] |
| AuNPs/GCE | DPASV | 62.1–290 | 62.0 | [61] |
| MIL-100(Cr)/GCE | SWASV | 207–2070 | 9.94 | [62] |
| TBA/MCH-Au | SWASV | 10.4–207 | 7.18 | [63] |
| BiNPs/GCE | SWASV | 5.00–60 | 0.80 | [64] |
| $\text{Bi}_2\text{O}_3/\text{MnO}_2/\text{GO}/\text{GCE}$ | SWASV | 2.07–2072 | 0.41 | This work |

3.7. Anti-Interference Ability

Excellent selectivity is essential for trace determination of HMIs in complex sample matrix. Therefore, the anti-interfering ability of the $\text{Bi}_2\text{O}_3/\text{MnO}_2/\text{GO}/\text{GCE}$ was also studied. To explore the anti-interfering ability, the SWASV responses of 1.0 μM Pb^{2+} were recorded on the $\text{Bi}_2\text{O}_3/\text{MnO}_2/\text{GO}/\text{GCE}$ in presence of 100-fold concentration interfering species, such as common cations (i.e., Na^+ , K^+ , Ca^{2+} , Mg^{2+} , Zn^{2+} , Fe^{2+} , Co^{2+} , Cu^{2+} , Cd^{2+} , Al^{3+}) and anions (i.e., Cl^- , NO_3^- , SO_4^{2-} , PO_4^{3-}). The relative errors are less than 5% in presence of these potential interfering species (Table S1), indicating that the $\text{Bi}_2\text{O}_3/\text{MnO}_2/\text{GO}/\text{GCE}$ possesses excellent selectivity. The extraordinary selectivity of the $\text{Bi}_2\text{O}_3/\text{MnO}_2/\text{GO}/\text{GCE}$ may due to the higher affinity of $\text{Bi}_2\text{O}_3/\text{MnO}_2/\text{GO}$ for Pb^{2+} . Interestingly, a sharp stripping peak of Cd^{2+} was also observed at -0.865 V on the $\text{Bi}_2\text{O}_3/\text{MnO}_2/\text{GO}/\text{GCE}$. In addition, the stripping peaks of Pb^{2+} and Cd^{2+} did not overlap each other with a broad potential separation of 0.215 V, suggesting the feasibility of simultaneous detection of Pb^{2+} and Cd^{2+} .

3.8. Reproducibility, Repeatability and Stability

To assess the practicability of the Bi₂O₃/MnO₂/GO/GCE composite, we also studied their reproducibility, repeatability, and stability. The relative standard deviation (RSD) for parallel detections of 10 μM of Pb²⁺ using five independent Bi₂O₃/MnO₂/GO/GCEs was 4.59% (Figure S2), indicating satisfactory reproducibility. The RSD for five consecutive detections of 10 μM of Pb²⁺ was 5.38% (Figure S3), suggesting admirable repeatability. Moreover, the I_{pa} of 10 μM of Pb²⁺ retained 92.05% of its initial values after one week (Figure S4), indicating excellent storage stability.

3.9. Determination of Trace Pb²⁺ in Water Samples

Under the optimal determination conditions, the Pb²⁺ concentrations in the water samples were quantitatively determined by the SWASV technique using the Bi₂O₃/MnO₂/GO/GCE composite. As summarized in Table 3, the Pb²⁺ concentration from a local lake was determined to be 0.121 μM, while no Pb²⁺ was determined in the tap water. To further confirm the accuracy and precision, a series of Pb²⁺ standard solutions of known concentrations were separately spiked into the water samples, and recovery assays were then performed. The Bi₂O₃/MnO₂/GO/GCE exhibited acceptable RSD values (3.83–5.89%) and satisfactory recoveries (95.5–105%). The Bi₂O₃/MnO₂/GO/GCE has demonstrated tremendous prospects in the sensitive determination of Pb²⁺ from complex matrixes.

Table 3. Determination of Pb²⁺ in the water samples using the Bi₂O₃/MnO₂/GO/GCE composite (*n* = 3).

| Samples | Detected (μM) | Added (μM) | Found (μM) | RSD (%) | Recovery (%) |
|------------|---------------|------------|------------|---------|--------------|
| Lake water | 0.121 | 0.100 | 0.226 | 5.89 | 105% |
| Lake water | 0.121 | 0.200 | 0.312 | 4.72 | 95.5% |
| Tap water | ND | 0.100 | 0.104 | 4.26 | 104% |
| Tap water | ND | 0.500 | 0.492 | 3.83 | 98.4% |

ND: not detected.

4. Conclusions

In this study, GO-coated binary transition metal oxides of Bi₂O₃/MnO₂ nanocomposites were used to fabricate a sensitive voltammetric sensor for the trace detection of lead ions in water samples. The Bi₂O₃/MnO₂/GO nanocomposites boosted the electroactive surface area and significantly reduced the charge transferred resistance. Moreover, the synergistic enhancement effect from the GO nanoflakes, dandelion-like α-MnO₂ microspheres, and flower-like β-Bi₂O₃ microspheres endowed Bi₂O₃/MnO₂/GO/GCE with extraordinary electrocatalytic activity toward the stripping voltammetric behavior of Pb²⁺. Under optimal detection conditions, the Bi₂O₃/MnO₂/GO/GCE exhibited a relatively wide LDR (0.01–10 μM), low LOD (2.0 nM) and high sensitivity (53.43 μA μM⁻¹). Moreover, the Bi₂O₃/MnO₂/GO/GCE exhibited an anti-interference ability even in presence of a 100-fold concentration of common cations and anions, as well as outstanding reproducibility, repeatability, and stability. The MnO₂/Bi₂O₃/GO/GCE composite realized the sensitive detection of trace Pb²⁺ in water samples with satisfactory recovery. Together with portable and smart electrochemical devices, the proposed Bi₂O₃/MnO₂/GO nanocomposites demonstrate promising prospects in the in situ detection of HMIs.

Supplementary Materials: The following supporting information can be downloaded at <https://www.mdpi.com/article/10.3390/nano12193317/s1>: Figure S1: The SWASV curves for the Bi₂O₃/MnO₂/GO/GCE recorded in the absence of Pb²⁺ (0.1 M HAc-NaAc buffer, pH = 5.5); Figure S2: The stripping peak current for parallel detections of 10 μM of Pb²⁺ using five independent Bi₂O₃/MnO₂/GO/GCEs; Figure S3: The stripping peak current for five consecutive detections of 10 μM of Pb²⁺ using the same Bi₂O₃/MnO₂/GO/GCE; Figure S4: The change in the stripping peak current of 10 μM

of Pb^{2+} within a week; and Table S1: The interference of selected ions on the determination of Pb^{2+} with $Bi_2O_3/MnO_2/GO/GCE$.

Author Contributions: Conceptualization, G.L. and C.Y.; methodology, G.L., X.Q. and Y.X. (Yonghui Xia); validation, Y.X. (Yang Xiao) and Y.Z.; formal analysis, X.W. and J.W.; investigation, G.L. and X.Q.; writing—original draft preparation, G.L. and C.Y.; writing—review and editing, C.Y.; visualization, G.L. and Y.X. (Yonghui Xia); project administration, K.L.; funding acquisition, G.L., K.L., Y.X. (Yang Xiao), Y.X. (Yonghui Xia) and C.Y.; All authors have read and agreed to the published version of the manuscript.

Funding: This research was funded by the Hunan Provincial Natural Science Foundation (Grant No. 2022JJ80123 and 2020JJ5126), Scientific Research Fund of Hunan Provincial Education Department (Grant No. 21B0532 and 20C0644), Zhuzhou Municipal Science and Technology Bureau (Grant No. 2020015) and Innovation and Entrepreneurship Training Program for College Students in Hunan Province (Grant No. S202111535026).

Institutional Review Board Statement: Not applicable.

Informed Consent Statement: Not applicable.

Data Availability Statement: The data are available upon reasonable request from the corresponding author.

Conflicts of Interest: The authors declare no conflict of interest.

References

1. Guo, H.; Wang, D.; Chen, J.; Weng, W.; Huang, M.; Zheng, Z. Simple fabrication of flake-like NH_2 -MIL-53(Cr) and its application as an electrochemical sensor for the detection of Pb^{2+} . *Chem. Eng. J.* **2016**, *289*, 479–485. [[CrossRef](#)]
2. Hwang, J.-H.; Wang, X.; Zhao, D.; Rex, M.M.; Cho, H.J.; Lee, W.H. A novel nanoporous bismuth electrode sensor for in situ heavy metal detection. *Electrochim. Acta* **2019**, *298*, 440–448. [[CrossRef](#)]
3. Steenland, K.; Boffetta, P. Lead and cancer in humans: Where are we now? *Am. J. Ind. Med.* **2000**, *38*, 295–299. [[CrossRef](#)]
4. Beltrán, B.; Leal, L.O.; Ferrer, L.; Cerdà, V. Determination of lead by atomic fluorescence spectrometry using an automated extraction/pre-concentration flow system. *J. Anal. At. Spectrom.* **2015**, *30*, 1072–1079. [[CrossRef](#)]
5. Sengan, M.; Kamlekar, R.K.; Veerappan, A. Highly selective rapid colorimetric sensing of Pb^{2+} ion in water samples and paint based on metal induced aggregation of N-decanoyltromethamine capped gold nanoparticles. *Spectrochim. Acta A* **2020**, *239*, 118485. [[CrossRef](#)] [[PubMed](#)]
6. Ghaedi, M.; Ahmadi, F.; Shokrollahi, A. Simultaneous preconcentration and determination of copper, nickel, cobalt and lead ions content by flame atomic absorption spectrometry. *J. Hazard. Mater.* **2007**, *142*, 272–278. [[CrossRef](#)]
7. Townsend, A.T.; Miller, K.A.; McLean, S.; Aldous, S. The determination of copper, zinc, cadmium and lead in urine by high resolution ICP-MS. *J. Anal. At. Spectrom.* **1998**, *13*, 1213–1219. [[CrossRef](#)]
8. Kagaya, S.; Mizuno, T.; Tohda, K. Inductively coupled plasma atomic emission spectrometric determination of 27 trace elements in table salts after coprecipitation with indium phosphate. *Talanta* **2009**, *79*, 512–516. [[CrossRef](#)] [[PubMed](#)]
9. Li, Q.; Wu, J.-T.; Liu, Y.; Qi, X.-M.; Jin, H.-G.; Yang, C.; Liu, J.; Li, G.-L.; He, Q.-G. Recent advances in black phosphorus-based electrochemical sensors: A review. *Anal. Chim. Acta* **2021**, *1170*, 338480. [[CrossRef](#)] [[PubMed](#)]
10. Sawan, S.; Maalouf, R.; Errachid, A.; Jaffrezic-Renault, N. Metal and metal oxide nanoparticles in the voltammetric detection of heavy metals: A review. *TrAC Trends Anal. Chem.* **2020**, *131*, 116014. [[CrossRef](#)]
11. Economou, A.; Fielden, P.R. Mercury film electrodes: Developments, trends and potentialities for electroanalysis. *Analyst* **2003**, *128*, 205–213. [[CrossRef](#)] [[PubMed](#)]
12. Shen, Y.; Li, X.; Chen, W.; Cheng, F.; Song, F. Electrochemical determination of indole butyric acid by differential pulse voltammetry on hanging mercury drops electrode. *J. Plant Biochem. Biotechnol.* **2013**, *22*, 319–323. [[CrossRef](#)]
13. Lezi, N.; Economou, A.; Dimovasilis, P.A.; Trikalitis, P.N.; Prodromidis, M.I. Disposable screen-printed sensors modified with bismuth precursor compounds for the rapid voltammetric screening of trace $Pb(II)$ and $Cd(II)$. *Anal. Chim. Acta* **2012**, *728*, 1–8. [[CrossRef](#)] [[PubMed](#)]
14. Švancara, I.; Prior, C.; Hočevar, S.B.; Wang, J. A Decade with Bismuth-Based Electrodes in Electroanalysis. *Electroanalysis* **2010**, *22*, 1405–1420. [[CrossRef](#)]
15. Hu, J.-S.; Zhong, L.-S.; Song, W.-G.; Wan, L.-J. Synthesis of Hierarchically Structured Metal Oxides and their Application in Heavy Metal Ion Removal. *Adv. Mater.* **2008**, *20*, 2977–2982. [[CrossRef](#)]
16. Jin, W.; Fu, Y.; Hu, M.; Wang, S.; Liu, Z. Highly efficient SnS-decorated Bi_2O_3 nanosheets for simultaneous electrochemical detection and removal of $Cd(II)$ and $Pb(II)$. *J. Electroanal. Chem.* **2020**, *856*, 113744. [[CrossRef](#)]
17. Ma, S.-B.; Nam, K.-W.; Yoon, W.-S.; Yang, X.-Q.; Ahn, K.-Y.; Oh, K.-H.; Kim, K.-B. Electrochemical properties of manganese oxide coated onto carbon nanotubes for energy-storage applications. *J. Power Sources* **2008**, *178*, 483–489. [[CrossRef](#)]

18. Li, Q.; Xia, Y.; Wan, X.; Yang, S.; Cai, Z.; Ye, Y.; Li, G. Morphology-dependent MnO₂/nitrogen-doped graphene nanocomposites for simultaneous detection of trace dopamine and uric acid. *Mater. Sci. Eng. C* **2020**, *109*, 110615. [[CrossRef](#)]
19. Su, Q.; Pan, B.; Wan, S.; Zhang, W.; Lv, L. Use of hydrous manganese dioxide as a potential sorbent for selective removal of lead, cadmium, and zinc ions from water. *J. Colloid Interface Sci.* **2010**, *349*, 607–612. [[CrossRef](#)]
20. Tripathy, S.S.; Bersillon, J.-L.; Gopal, K. Adsorption of Cd²⁺ on hydrous manganese dioxide from aqueous solutions. *Desalination* **2006**, *194*, 11–21. [[CrossRef](#)]
21. Wang, L.; Lei, T.; Ren, Z.; Jiang, X.; Yang, X.; Bai, H.; Wang, S. Fe₃O₄@PDA@MnO₂ core-shell nanocomposites for sensitive electrochemical detection of trace Pb(II) in water. *J. Electroanal. Chem.* **2020**, *864*, 114065. [[CrossRef](#)]
22. Zhang, Q.-X.; Wen, H.; Peng, D.; Fu, Q.; Huang, X.-J. Interesting interference evidences of electrochemical detection of Zn(II), Cd(II) and Pb(II) on three different morphologies of MnO₂ nanocrystals. *J. Electroanal. Chem.* **2015**, *739*, 89–96. [[CrossRef](#)]
23. Mališić, M.; Janošević, A.; Šljukić Paunković, B.; Stojković, I.; Ćirić-Marjanović, G. Exploration of MnO₂/carbon composites and their application to simultaneous electroanalytical determination of Pb(II) and Cd(II). *Electrochim. Acta* **2012**, *74*, 158–164. [[CrossRef](#)]
24. Wang, J.; Yang, X.; Zhao, K.; Xu, P.; Zong, L.; Yu, R.; Wang, D.; Deng, J.; Chen, J.; Xing, X. Precursor-induced fabrication of β-Bi₂O₃ microspheres and their performance as visible-light-driven photocatalysts. *J. Mater. Chem. A* **2013**, *1*, 9069–9074. [[CrossRef](#)]
25. Li, L.; Ma, D.-K.; Qi, F.; Chen, W.; Huang, S. Bi nanoparticles/Bi₂O₃ nanosheets with abundant grain boundaries for efficient electrocatalytic CO₂ reduction. *Electrochim. Acta* **2019**, *298*, 580–586. [[CrossRef](#)]
26. Mane, S.A.; Kashale, A.A.; Kamble, G.P.; Kolekar, S.S.; Dhas, S.D.; Patil, M.D.; Moholkar, A.V.; Sathe, B.R.; Ghule, A.V. Facile synthesis of flower-like Bi₂O₃ as an efficient electrode for high performance asymmetric supercapacitor. *J. Alloys Compd.* **2022**, *926*, 166722. [[CrossRef](#)]
27. Yang, S.; Qian, L.; Ping, Y.; Zhang, H.; Li, J.; Xiong, B.; Fang, P.; He, C. Electrochemical performance of Bi₂O₃ supercapacitors improved by surface vacancy defects. *Ceram. Int.* **2021**, *47*, 8290–8299. [[CrossRef](#)]
28. Li, J.; Chen, D.; Zhang, Q.; Zhang, Y.; Wang, X.; Yang, C.; Wu, Q. Synthesis of Sponge-Like Bi₂O₃ by Using a Soft/Hard-Combined Biomembrane Support System for Application as Supercapacitor. *Eur. J. Inorg. Chem.* **2018**, *2018*, 1688–1692. [[CrossRef](#)]
29. Manjula, N.; Chen, T.-W.; Chen, S.-M.; Lou, B.-S. Sonochemical Synthesis and Characterization of Rod-Shaped Bi₂O₃/ZnO Anchored with f-MWCNT Nanocomposite for the Electrochemical Determination of Ofloxacin. *J. Electrochem. Soc.* **2021**, *168*, 087506. [[CrossRef](#)]
30. Li, G.; Qi, X.; Zhang, G.; Wang, S.; Li, K.; Wu, J.; Wan, X.; Liu, Y.; Li, Q. Low-cost voltammetric sensors for robust determination of toxic Cd(II) and Pb(II) in environment and food based on shuttle-like α-Fe₂O₃ nanoparticles decorated β-Bi₂O₃ microspheres. *Microchem. J.* **2022**, *179*, 107515. [[CrossRef](#)]
31. Zeinu, K.M.; Hou, H.; Liu, B.; Yuan, X.; Huang, L.; Zhu, X.; Hu, J.; Yang, J.; Liang, S.; Wu, X. A novel hollow sphere bismuth oxide doped mesoporous carbon nanocomposite material derived from sustainable biomass for picomolar electrochemical detection of lead and cadmium. *J. Mater. Chem. A* **2016**, *4*, 13967–13979. [[CrossRef](#)]
32. Pauliukaite, R.; Metelka, R.; Švancara, I.; Królicka, A.; Bobrowski, A.; Vytřas, K.; Norkus, E.; Kalcher, K. Carbon paste electrodes modified with Bi₂O₃ as sensors for the determination of Cd and Pb. *Anal. Bioanal. Chem.* **2002**, *374*, 1155–1158. [[CrossRef](#)] [[PubMed](#)]
33. Pérez, M.A.; López Teijelo, M. Cathodic behavior of bismuth. I. Ellipsometric study of the electroreduction of thin Bi₂O₃ films. *J. Electroanal. Chem.* **2005**, *583*, 212–220. [[CrossRef](#)]
34. Wei, L.; Karahan, H.E.; Zhai, S.; Liu, H.; Chen, X.; Zhou, Z.; Lei, Y.; Liu, Z.; Chen, Y. Amorphous Bimetallic Oxide–Graphene Hybrids as Bifunctional Oxygen Electrocatalysts for Rechargeable Zn–Air Batteries. *Adv. Mater.* **2017**, *29*, 1701410. [[CrossRef](#)] [[PubMed](#)]
35. Chen, D.; Chen, C.; Baiyee, Z.M.; Shao, Z.; Ciucci, F. Nonstoichiometric Oxides as Low-Cost and Highly-Efficient Oxygen Reduction/Evolution Catalysts for Low-Temperature Electrochemical Devices. *Chem. Rev.* **2015**, *115*, 9869–9921. [[CrossRef](#)]
36. Pu, Y.; Wu, Y.; Yu, Z.; Lu, L.; Wang, X. Simultaneous determination of Cd²⁺ and Pb²⁺ by an electrochemical sensor based on Fe₃O₄/Bi₂O₃/C₃N₄ nanocomposites. *Talanta Open* **2021**, *3*, 100024. [[CrossRef](#)]
37. Wei, J.; Zhao, J.; Li, C.-Y.; Xie, X.-Y.; Wei, Y.-Y.; Shen, W.; Wang, J.-P.; Yang, M. Highly sensitive and selective electrochemical detection of Pb(II) in serum via an α-Fe₂O₃/NiO heterostructure: Evidence from theoretical calculations and adsorption investigation. *Sens. Actuators B Chem.* **2021**, *344*, 130295. [[CrossRef](#)]
38. Das, T.R.; Sharma, P.K. Sensitive and selective electrochemical detection of Cd²⁺ by using bimetal oxide decorated Graphene oxide (Bi₂O₃/Fe₂O₃@GO) electrode. *Microchem. J.* **2019**, *147*, 1203–1214. [[CrossRef](#)]
39. Shaikh, Z.A.; Shinde, P.V.; Shaikh, S.F.; Al-Enizi, A.M.; Mane, R.S. Facile synthesis of Bi₂O₃@MnO₂ nanocomposite material: A promising electrode for high performance supercapacitors. *Solid State Sci.* **2020**, *102*, 106158. [[CrossRef](#)]
40. Ng, C.H.; Lim, H.N.; Hayase, S.; Zainal, Z.; Shafie, S.; Huang, N.M. Effects of Temperature on Electrochemical Properties of Bismuth Oxide/Manganese Oxide Pseudocapacitor. *Ind. Eng. Chem. Res.* **2018**, *57*, 2146–2154. [[CrossRef](#)]
41. Ray, C.; Dutta, S.; Roy, A.; Sahoo, R.; Pal, T. Redox mediated synthesis of hierarchical Bi₂O₃/MnO₂ nanoflowers: A non-enzymatic hydrogen peroxide electrochemical sensor. *Dalton Trans.* **2016**, *45*, 4780–4790. [[CrossRef](#)] [[PubMed](#)]
42. Zheng, D.; Hu, H.; Liu, X.; Hu, S. Application of graphene in electrochemical sensing. *Curr. Opin. Colloid Interface Sci.* **2015**, *20*, 383–405. [[CrossRef](#)]

43. Liu, J.; Liu, W.; Wang, Y.; Xu, M.; Wang, B. A novel reusable nanocomposite adsorbent, xanthated Fe₃O₄-chitosan grafted onto graphene oxide, for removing Cu(II) from aqueous solutions. *Appl. Surf. Sci.* **2016**, *367*, 327–334. [[CrossRef](#)]
44. Heitzmann, M.; Bucher, C.; Moutet, J.-C.; Pereira, E.; Rivas, B.L.; Royal, G.; Saint-Aman, E. Complexation of poly(pyrrole-EDTA like) film modified electrodes: Application to metal cations electroanalysis. *Electrochim. Acta* **2007**, *52*, 3082–3087. [[CrossRef](#)]
45. Huang, W.; Zhang, Y.; Li, Y.; Zeng, T.; Wan, Q.; Yang, N. Morphology-controlled electrochemical sensing of environmental Cd²⁺ and Pb²⁺ ions on expanded graphite supported CeO₂ nanomaterials. *Anal. Chim. Acta* **2020**, *1126*, 63–71. [[CrossRef](#)]
46. Zhang, Q.-X.; Peng, D.; Huang, X.-J. Effect of morphology of α-MnO₂ nanocrystals on electrochemical detection of toxic metal ions. *Electrochem. Commun.* **2013**, *34*, 270–273. [[CrossRef](#)]
47. Zheng, X.; Yu, L.; Lan, B.; Cheng, G.; Lin, T.; He, B.; Ye, W.; Sun, M.; Ye, F. Three-dimensional radial α-MnO₂ synthesized from different redox potential for bifunctional oxygen electrocatalytic activities. *J. Power Sources* **2017**, *362*, 332–341. [[CrossRef](#)]
48. Li, G.; Wu, J.; Jin, H.; Xia, Y.; Liu, J.; He, Q.; Chen, D. Titania/Electro-Reduced Graphene Oxide Nanohybrid as an Efficient Electrochemical Sensor for the Determination of Allura Red. *Nanomaterials* **2020**, *10*, 307. [[CrossRef](#)]
49. He, Q.; Liu, J.; Liu, X.; Li, G.; Deng, P.; Liang, J. Manganese dioxide Nanorods/electrochemically reduced graphene oxide nanocomposites modified electrodes for cost-effective and ultrasensitive detection of Amaranth. *Colloids Surf. B* **2018**, *172*, 565–572. [[CrossRef](#)]
50. Li, G.; Wang, S.; Li, M.; Duan, Y.Y. Towards real-life EEG applications: Novel superporous hydrogel-based semi-dry EEG electrodes enabling automatically ‘charge–discharge’ electrolyte. *J. Neural Eng.* **2021**, *18*, 046016. [[CrossRef](#)]
51. Li, G.; Ren, M.; Zhou, H. Observably boosted electrochemical performances of roughened graphite sheet/polyaniline electrodes for use in flexible supercapacitors. *Surf. Interfaces* **2022**, *30*, 101874. [[CrossRef](#)]
52. Li, G.; Wu, J.; Xia, Y.; He, Q.; Jin, H. Review of semi-dry electrodes for EEG recording. *J. Neural Eng.* **2020**, *17*, 051004. [[CrossRef](#)] [[PubMed](#)]
53. Li, G.; Qi, X.; Wu, J.; Xu, L.; Wan, X.; Liu, Y.; Chen, Y.; Li, Q. Ultrasensitive, label-free voltammetric determination of norfloxacin based on molecularly imprinted polymers and Au nanoparticle-functionalized black phosphorus nanosheet nanocomposite. *J. Hazard. Mater.* **2022**, *436*, 129107. [[CrossRef](#)]
54. Li, G.; Wu, J.; Qi, X.; Wan, X.; Liu, Y.; Chen, Y.; Xu, L. Molecularly imprinted polypyrrole film-coated poly(3,4-ethylenedioxythiophene):polystyrene sulfonate-functionalized black phosphorene for the selective and robust detection of norfloxacin. *Mater. Today Chem.* **2022**, *26*, 101043. [[CrossRef](#)]
55. Ping, J.; Wang, Y.; Wu, J.; Ying, Y. Development of an electrochemically reduced graphene oxide modified disposable bismuth film electrode and its application for stripping analysis of heavy metals in milk. *Food Chem.* **2014**, *151*, 65–71. [[CrossRef](#)] [[PubMed](#)]
56. Zhou, W.; Li, C.; Sun, C.; Yang, X. Simultaneously determination of trace Cd²⁺ and Pb²⁺ based on L-cysteine/graphene modified glassy carbon electrode. *Food Chem.* **2016**, *192*, 351–357. [[CrossRef](#)]
57. Yao, Y.; Wu, H.; Ping, J. Simultaneous determination of Cd(II) and Pb(II) ions in honey and milk samples using a single-walled carbon nanohorns modified screen-printed electrochemical sensor. *Food Chem.* **2019**, *274*, 8–15. [[CrossRef](#)] [[PubMed](#)]
58. Maleki, B.; Baghayeri, M.; Ghanei-Motlagh, M.; Mohammadi Zonoz, F.; Amiri, A.; Hajizadeh, F.; Hosseini, A.; Esmaeilnezhad, E. Polyamidoamine dendrimer functionalized iron oxide nanoparticles for simultaneous electrochemical detection of Pb²⁺ and Cd²⁺ ions in environmental waters. *Measurement* **2019**, *140*, 81–88. [[CrossRef](#)]
59. Yang, Z.-H.; Wu, X.-Y.; Liu, X.-C.; Xu, M.-M. One-step Bridging of g-C₃N₄ and Graphene Oxide by Successive Electrolysis for Constructing Electrochemical Sensor of Pb²⁺. *Chin. J. Anal. Chem.* **2021**, *49*, e21179–e21186. [[CrossRef](#)]
60. Nie, J.; He, B.; Cheng, Y.; Yin, W.; Hou, C.; Huo, D.; Qian, L.; Qin, Y.; Fa, H. Design of L-cysteine functionalized Au@SiO₂@Fe₃O₄/nitrogen-doped graphene nanocomposite and its application in electrochemical detection of Pb²⁺. *Chem. Res. Chin. Univ.* **2017**, *33*, 951–957. [[CrossRef](#)]
61. Xu, X.; Duan, G.; Li, Y.; Liu, G.; Wang, J.; Zhang, H.; Dai, Z.; Cai, W. Fabrication of Gold Nanoparticles by Laser Ablation in Liquid and Their Application for Simultaneous Electrochemical Detection of Cd²⁺, Pb²⁺, Cu²⁺, Hg²⁺. *ACS Appl. Mater. Interfaces* **2014**, *6*, 65–71. [[CrossRef](#)]
62. Wang, D.; Ke, Y.; Guo, D.; Guo, H.; Chen, J.; Weng, W. Facile fabrication of cauliflower-like MIL-100(Cr) and its simultaneous determination of Cd²⁺, Pb²⁺, Cu²⁺ and Hg²⁺ from aqueous solution. *Sens. Actuators B* **2015**, *216*, 504–510. [[CrossRef](#)]
63. Jarczewska, M.; Kierzkowska, E.; Ziółkowski, R.; Górski, Ł.; Malinowska, E. Electrochemical oligonucleotide-based biosensor for the determination of lead ion. *Bioelectrochemistry* **2015**, *101*, 35–41. [[CrossRef](#)] [[PubMed](#)]
64. Yang, D.; Wang, L.; Chen, Z.; Megharaj, M.; Naidu, R. Anodic stripping voltammetric determination of traces of Pb (II) and Cd (II) using a glassy carbon electrode modified with bismuth nanoparticles. *Microchim. Acta* **2014**, *181*, 1199–1206. [[CrossRef](#)]